Supplementary Information for

Atomic indium oxide domains redirect zinc selectivity for exclusive CO_2-to-formate conversion

Jing Xue[1,2†], Jun Long[3,†], Yizhen Chen[4], Runhao Zhang[2], Yanjiang Wang[2], Chengbo Li[1], Chunxiao Liu[1], Sunpei Hu[2], Yuan Ji[1], Xu Li[1], Chih-Wen Pao[5], Qunxiang Li[2], Jie Zeng[2,6], Tingting Zheng[1], Jianping Xiao[3*], Chuan Xia[1*]

[1]School of Materials and Energy, University of Electronic Science and Technology of China, Chengdu 611731, P. R. China

[2]Hefei National Research Center for Physical Sciences at the Microscale, Key Laboratory of Strongly-Coupled Quantum Matter Physics of Chinese Academy of Sciences, Key Laboratory of Surface and Interface Chemistry and Energy Catalysis of Anhui Higher Education Institutes, Department of Chemical Physics, University of Science and Technology of China, Hefei, Anhui 230026, P. R. China

[3]State Key Laboratory of Catalysis, Dalian Institute of Chemical Physics, Chinese Academy of Sciences, Dalian National Laboratory for Clean Energy, Dalian 116023, P. R. China

[4]Department of Chemical Engineering, University of California, Davis, California 95616, United States

[5]National Synchrotron Radiation Research Center, Hsinchu, Taiwan

[6]School of Chemistry & Chemical Engineering, Anhui University of Technology, Ma'anshan, Anhui 243002, P. R. China

*Corresponding author: E-mail: xiao@dicp.ac.cn; chuan.xia@uestc.edu.cn

†These authors contributed equally to this work.

Experimental Section

Materials

Zinc nitrate hexahydrate ($Zn(NO_3)_2 \cdot 6H_2O$, 99%) was purchased from KESHI. Indium(III) chloride tetrahydrate ($InCl_3 \cdot 4H_2O$, 99.99%), sodium borohydride ($NaBH_4$, 97%), ethanol (EtOH, 99.7%) and isopropanol (IPA, 99.5%) were purchased from Macklin. Potassium hexafluorophosphate (KF_6P, 99%) and acetonitrile (MeCN, 99.9%) were obtained from Sigma-Aldrich. All the chemicals were used without further purification.

Preparation of catalysts

The In_1(O)Zn catalyst is synthesized by directly reducing water-dissolved $InCl_3$ and $Zn(NO_3)_2$ precursors with a $NaBH_4$ solution. The details are as follows. Solution A was prepared by dissolving 17.6 mg of $InCl_3 \cdot 4H_2O$ and 339 mg of $Zn(NO_3)_2 \cdot 6H_2O$ in deionized water. The mixture was subsequently sonicated for 15 min to obtain a clear solution. Later, 0.95 g of $NaBH_4$ was dissolved in 10 mL of deionized water (DI) at 0 °C to prepare solution B. Afterwards, solution A was rapidly added to solution B in a beaker at 0 ℃ with continuous stirring for 45 min in air. After the vigorous reaction subsided, the resulting white precipitate was washed with DI water and EtOH three times and dried under vacuum at room temperature for 6 hours. The obtained samples were then stored in a glove box under an Ar atmosphere.

Characterizations

Transmission electron microscopy (TEM) images and energy dispersive X-ray (EDX) elemental mapping were obtained on a Tecnai G2 F20 S-TWIN using Mo-based TEM grids. High-angle annular dark-field scanning transmission electron microscopy (HAADF-STEM) images and corresponding energy-dispersive spectroscopy (EDS) elemental mapping were measured on a JEOL ARM-200F field-emission transmission electron microscope operated at 200 kV using Mo-based TEM grids. X-ray photoelectron spectroscopy (XPS) measurements were performed on a Kratos-Axis Supra XPS spectrometer with an excitation source of Al Kα = 1486.6 eV. The binding energies obtained from the XPS spectral analysis were corrected by referencing C 1*s* to 284.6 eV. The *in situ* X-ray absorption spectra (XAS) of the Zn *K*-edges and In *K*-edges were obtained at the BL11B and BL14W1 beamlines at the Shanghai Synchrotron Radiation Facility (SSRF) in “top-up” mode with a constant current of 200 mA, and

recorded in fluorescence mode in an H-cell with a Lytle detector. *Ex situ* XAS of In *K*-edges was conducted at the Taiwan Photon Source (beamline 44A). Before *ex situ* characterization, the sample was pre-reduced for 30 min at a current density of -200 mA cm^{-2} under a CO_2 atmosphere. All the spectra were processed and analysed with the software codes Athena and Artemis. *In situ* Raman analysis was performed using a Renishaw inVia Raman analyser equipped with 532- and 633-nm lasers combined with a custom flow cell. During the experiments, the laser was focused on the surface of the sample with a laser intensity of 10%~25%. *In situ* electrochemical attenuated total reflection surface-enhanced infrared absorption spectroscopy (ATR-SEIRAS) experiments were conducted on a Thermo Scientific Nicolet iS50 FTIR spectrometer at room temperature. Si crystals were used in the ATR-SEIRAS experiments. Before the experiments, a polycrystalline Au film was deposited onto the Si crystal *via* chemical bath deposition. Typically, the polished Si crystal was first immersed in an NH_4F bath for 2 minutes. Au plating solutions with 5.75 mM $NaAuCl_4 \cdot 2H_2O$, 0.025 M NH_4Cl, 0.025 M $Na_2S_2O_3 \cdot 5H_2O$ (98%), 0.075 M Na_2SO_3 (98%), and 0.026 M NaOH (99.99%) were prepared. Then, 0.8 mL of 2 wt% HF aqueous solution was mixed with 4.4 mL of the above Au plating solution, after which the Si surface was immersed in the above mixed solution for 15 min at 55 °C and later rinsed with water. After the above preparation process, the precursor ink was spray-coated onto the Au film by an air brush for further use. TPR-H_2 measurements were conducted on an Xianquan TP-5080 under a H_2/Ar mixture of 10%:90% with a flow rate of 50 mL min^{-1}. H_2 consumption and H_2O generation were synchronously monitored using a Hiden Analytical DECRA Mass Spectrometer.

Electrochemical measurements

CO_2RR performance test

All the electrochemical measurements were conducted at room temperature using a BioLogic VMP3 or CHI (1140c). Typical three-electrode cell measurements were performed using a conventional flow cell. To prepare the cathode electrode, precursor ink (12 mg of catalyst mixed with 24 μL of 5% Nafion 117 solution dissolved in 2 mL of IPA) was spray-coated onto a gas diffusion layer (YLS-30T) with a mass loading of ~1 mg cm^{-2} using an air brush, and was subsequently dried in air on a hotplate at 60 °C. The Ag/AgCl wire in saturated KCl solution was used as the reference electrode, and Ni foam was used as the counter electrode. The working and counter electrodes were

then placed on opposite sides of two 1-cm-thick polytetrafluoroethylene (PTFE) sheets with 0.4 cm × 1.5 cm channels such that the catalyst layer interfaced with the flowing electrolyte. The geometric surface area of the catalyst was 0.6 cm^2. A Nafion 115 membrane (Fuel Cell Store) was sandwiched between the two PTFE sheets to separate the chambers. A schematic illustration of the flow-cell configuration is provided in Figure S28. CO_2 flowed through the gas room behind the cathode, and the flow rate was maintained at 30 sccm (monitored by an Alicat Scientific mass flow controller). A soap-film flowmeter was used to measure the CO_2 flow rate out of the flow-cell at high current densities. In addition, 0.5 M $KHCO_3$ (pH = 7.4 or 7.2 if CO_2 was saturated) was circulated as the cathode electrolyte at a flow rate of 1.8 mL min^{-1}, while 1 M KOH was purged as the anode electrolyte. All potentials measured using the three-electrode setup were converted to the RHE reference scale using the relation $E_{RHE} = E_{Ag/AgCl} + 0.197 + pH \times 0.0592 - i \times R$, where R is the solution resistance during flow cell operation. R was determined by potentiostatic electrochemical impedance spectroscopy. All potentials were manually compensated by iR correction. At least three independent measurements were carried out under each current.

CO_2RR product analysis

The gaseous products were tested by online gas chromatography (GC) (PerkinElmer Clarus 690), which was equipped with a flame ionization detector, a thermal conductivity detector, and a Molsieve 5 Å column. The liquid products were quantified by a 400 MHz nuclear magnetic resonance (NMR) spectrometer (BUKER) and ion chromatography (IC) (Thermo Fisher Scientific ICS-600). For the NMR tests, 100 μL of D_2O (Sigma Aldrich, 99.9%) and 0.05 μL of dimethyl sulfoxide (DMSO) (Sigma Aldrich, 99.9%) as an internal standard were added to 600 μL of the electrolyte after electrolysis.

ECSA measurements

ECSA measurements were conducted on a single-chamber electrolytic cell with 0.15 M KF_6P in MeCN as the electrolyte. The catalysts were loaded on glassy carbon electrodes, and Ni foam was used as the counter electrode. In ECSA measurements, the electrical double-layer capacitance (C_{dl}) is calculated by plotting the relationship of $\Delta j = ja - jc$, where ja and jc are the positive and negative scan currents, respectively. C_{dl} is derived from the slope of Δj as a function of the scan rate.

Tafel plot

Tafel plots were employed to evaluate the CO_2RR catalytic kinetics and fitted with the following equation: $\eta = k \times \lg(j_{formate}) + b$, where $j_{formate}$ is the formate partial current density and η is the overpotential for $CO_2 + H_2O + 2e^- \rightarrow HCOO^- + OH^-$ (E^0 = -0.02 V *vs.* RHE). A smaller slope k indicates faster kinetics toward formate production. If the rate-determining step (RDS) is the first electron transfer CO_2-to-$*CO_2^-$, the Tafel slope can be calculated by the following formula:

$$\frac{\partial(-\eta)}{\partial \lg(j_{formate})} = \frac{2.3RT}{\alpha F}$$

In this equation, α is the transfer coefficient, and F is the Faraday constant. The standard values of the Tafel slopes based on different RDSs are further given in Table S4[1].

FTacV measurements

FTacV experiments were conducted on a CHI 660e electrochemical workstation using an applied sine wave perturbation with an amplitude (ΔE) of 80 mV and a frequency (f) of 9.02 Hz superimposed onto the direct current (dc) ramp from 0 V to -1.20 V *vs.* RHE with a scan rate (v) of 10.57 mV s^{-1}. A standard three-electrode H-cell setup was used. Pt wire was used as the counter electrode, and Ag/AgCl was used as the reference electrode. All the catalysts were coated on glassy carbon as working electrodes, and 0.5 M $KHCO_3$ (pH = 7.4, or 7.2 if CO_2 was saturated) was used as the electrolyte. Before each measurement, the electrolyte was bubbled for at least 20 min with 40 sccm Argon or CO_2.

***In situ* electrochemical QCM measurement**

An EQCM (QCM-922, Princeton Applied Research, USA) equipped with an o-AT cut, gold/gold polished, 9 MHz quartz crystal (Seiko EG&G) was used to record the frequency change of the gold-coated quartz crystal electrode. All the EQCM measurements were performed using a CHI 660e electrochemical workstation. A standard three-electrode H-cell setup was used, with a Pt wire as the counter electrode, Ag/AgCl as the reference electrode and 0.5 M $KHCO_3$ (pH = 7.4) as the electrolyte. Before each measurement, the electrolyte was bubbled for at least 20 min with 40 sccm Argon to exclude dissolved CO_2. The weight loss can be calculated *via* the Sauerbrey equation:

$$\Delta mass = \frac{-\Delta freq \times Area \times sqrt(\mu q \times \rho q)}{2\,(Fq^2)}$$

where μq is the AT-cut quartz constant (2.947×10^{11} g/cm·s^2), ρq is the quartz crystal density (2.65 g/cm^3) and Fq is the reference frequency (9.00 MHz).

***In situ* DEMS measurement**

In situ differential electrochemical mass spectrometry (DEMS) was performed using a custom-made electrochemical capillary DEMS flow cell. The catalysts were loaded on the gas diffusion layer (GDL) as the cathode, where CO_2 flowed behind. In addition, 0.5 M $KHCO_3$ (pH = 7.4 or 7.2 if CO_2 was saturated) was used as the electrolyte. A capillary was inserted into the gas outlet of the flow cell to draw the gas products into the DEMS sensor (PrismaPro). The signals at mass-to-charge ratios (m/z) of 2, 26 and 28 represent H_2, C_2H_4 and CO, respectively. Linear sweep voltammetry (LSV) with a scan rate of 5 mV s^{-1} was conducted on the cathode.

LSV measurements in HER

LSV measurements were conducted on a CHI 660e electrochemical workstation with a scan rate of 5 mV s^{-1}. A standard three-electrode H-cell setup was used. Ni foam was used as the counter electrode, and Ag/AgCl was used as the reference electrode. All the catalysts were coated on glassy carbon as working electrodes, and 0.5 M $KHCO_3$ was used as the electrolyte. Before each measurement, the electrolyte was bubbled for at least 20 min with 40 sccm Argon.

Porous-state-electrolyte reactor for the CO_2RR

In a PSE device, the acidic oxygen evolution reaction (OER) at the anode is paired with the alkaline CO_2RR at the cathode. To set up a PSE reactor, an AEM (Dioxide Materials and Membranes International, Inc.) and Nafion film (Fuel Cell Store) were used for anion and cation exchange, respectively. Approximately 0.8 mg cm^{-2} catalyst loaded on a YLS-30T GDL electrode (4.0 cm^2 electrode area) was used as the cathode, and IrO_2 was loaded on a titanium mesh as the anode. CO_2 was directly fed to the GDL cathode at 40 sccm (monitored by an Alicat Scientific mass flow controller). The anode side was circulated with 0.5 M H_2SO_4 aqueous solution. The porous styrenedivinylbenzene sulfonated copolymer was used as the solid ion conductor. DI water was used to release the produced HCOOH within the PSE layer, and the flow rate was maintained at 1.2

mL min^{-1}. A schematic illustration and photograph of the PSE reactor is provided in Figure S22.

The full-cell energy efficiency of the PSE reactor can be calculated as follows:

$$\text{Energy efficiency} = (E_{anode} - E_{cathode})/E_{cell} \times FE_{HCOOH}$$

During the reaction, E_{anode} = 1.23 V versus standard hydrogen electrode (*vs.* SHE) under acidic condition, and $E_{cathode}$ = -0.639 V *vs.* SHE under alkaline condition. E_{cell} is the real cell voltage.

Computational details

All DFT calculations in this study were performed with the Vienna Ab initio Simulation Package[2,3], using the exchange-correlation functional of the revised Perdew-Burke-Ernzerhof (rPBE)[4] under the generalized-gradient approximation (GGA). The calculations of structural optimization were converged at 0.05 eV/Å of residual force. The cutoff energy was set to 400 eV, with a Gaussian smearing width of 0.2 eV. The DFT-D2 method was used to consider the Van der Waals interactions in the calculations[5]. A (3×3×1) of Monkhorst-Pack k-point mesh grid was employed for Brillouin zone sampling. The method of climbing-image nudged elastic band (CI-NEB) was adopted to find the reaction transition states for the calculation of the reaction barrier[6,7]. To keep the electrode potential of each image constant in calculation, a method of electric field controlling constant potential calculations (EFC-CP) was employed, which was developed in our recent work[8]. The Zn (101) and In (101) facets were used as the catalyst models of Zn and In in this work because they were proven to be the active surfaces for the CO_2RR[9,10,11]. In the framework of EFC-CP, the dielectric constant (ϵ_{HP}) of the Helmholtz layer in the catalyst-water model needs to be calculated *via* a fitting method and is determined to be 4.69, 9.50, and 4.77 for pristine-Zn, In_1(O)Zn, and In, respectively (Figure S29). In addition, the potentials of the internal reversible hydrogen electrode (ϕ_{IRHE}) of Zn, In_1(O)Zn, and In were determined to be -0.12, 0.49, and 0.21 V, respectively, relative to the potential of zero charge (ϕ_{PZC}) (Figure S30). The microkinetic simulations were performed with the CATKINAS developed by Chen *et al.*[12,13].

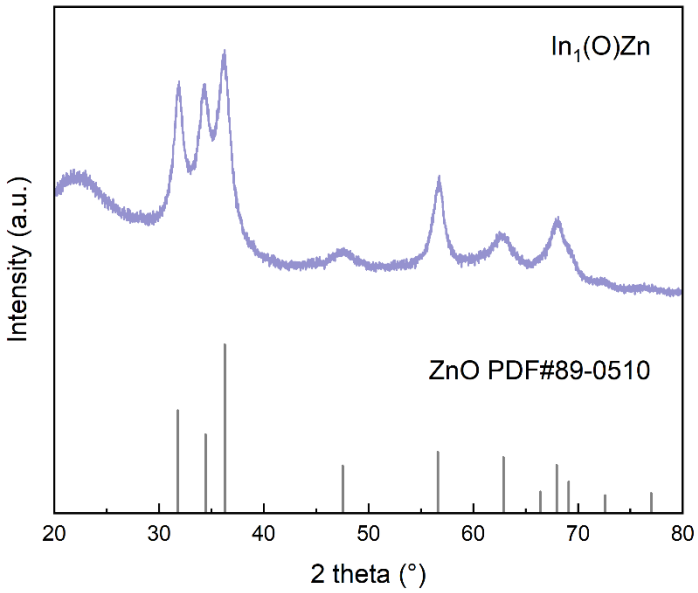

Figure S1. XRD pattern of the as-prepared In_1(O)Zn catalyst. Only ZnO diffraction peaks were observed (PDF#89-0510), confirming the absence of crystalline In or In_2O_3 phases.

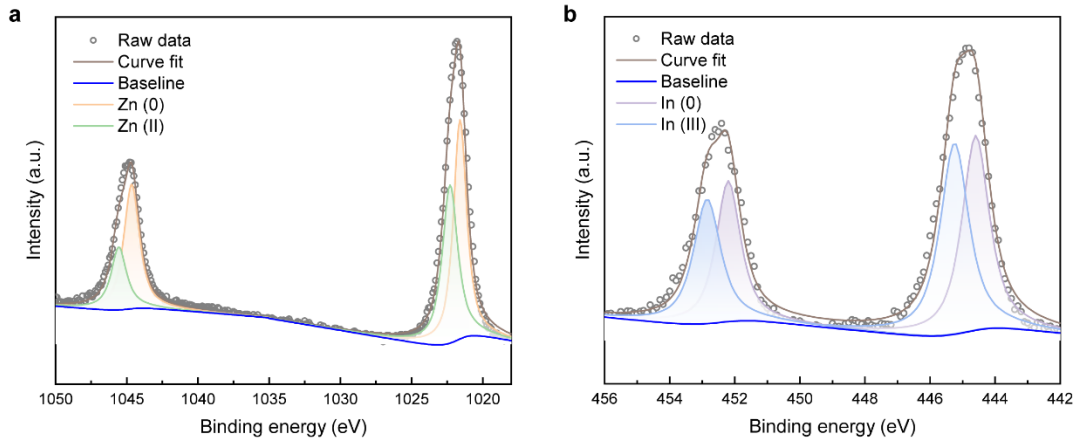

Figure S2. XPS spectra of the as-synthesized In_1(O)Zn catalyst. Zn 2*p* (a) and In 3*d* (b) spectra on the catalyst surface.

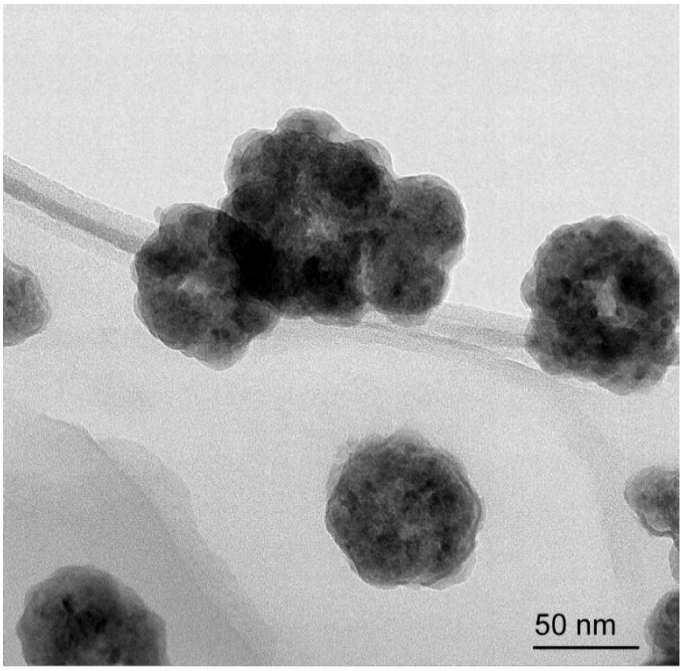

Figure S3. TEM images of the as-synthesized $In_1(O)Zn$ catalyst. The nanoparticle diameters ranged from 50 to 60 nm.

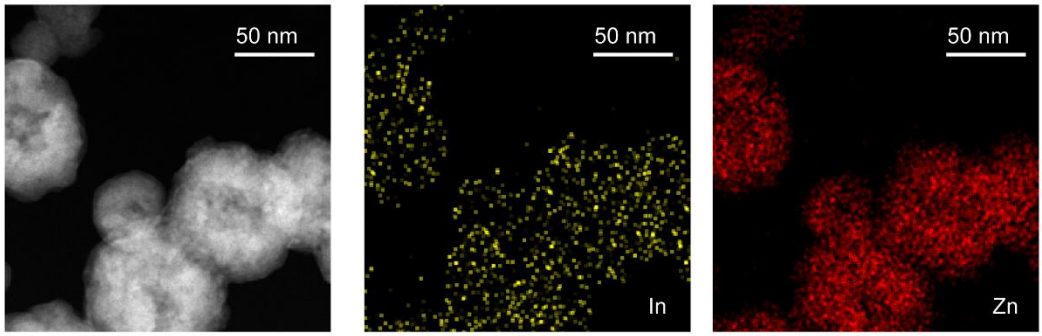

Figure S4. Large-scale EDS mapping of the as-synthesized In_1(O)Zn catalyst. No elemental segregation was detected, precluding the formation of In-rich clusters or nanoparticles.

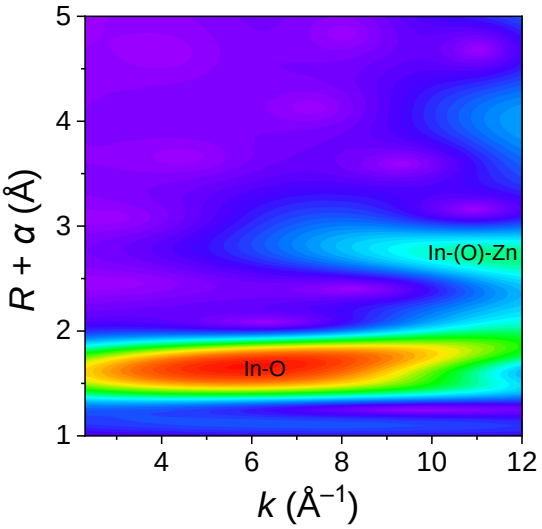

Figure S5. WT of the In *K*-edge EXAFS from the as-synthesized In$_1$(O)Zn catalyst. The WT profile displays two intensity maxima at approximately 6 and 11.5 Å^{-1} corresponding to In-O in In-(O)-Zn coordination, respectively, indicating the formation of In-O-Zn coordination in the as-prepared catalyst.

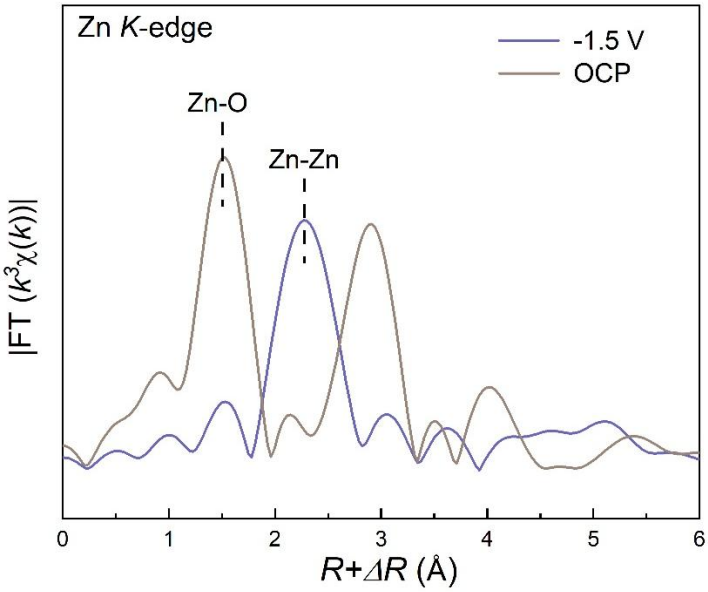

Figure S6. *Operando* Zn *K*-edge EXAFS of the In_1(O)Zn catalyst at -1.5 V *vs.* RHE during the CO_2RR. The catalyst was in a fully oxidized state at the open-circuit potential (OCP); however, upon prolonged electroreduction, it underwent partial reduction. A decrease in the number of Zn-O bonds and the appearance of Zn-Zn bonds in In_1(O)Zn were observed.

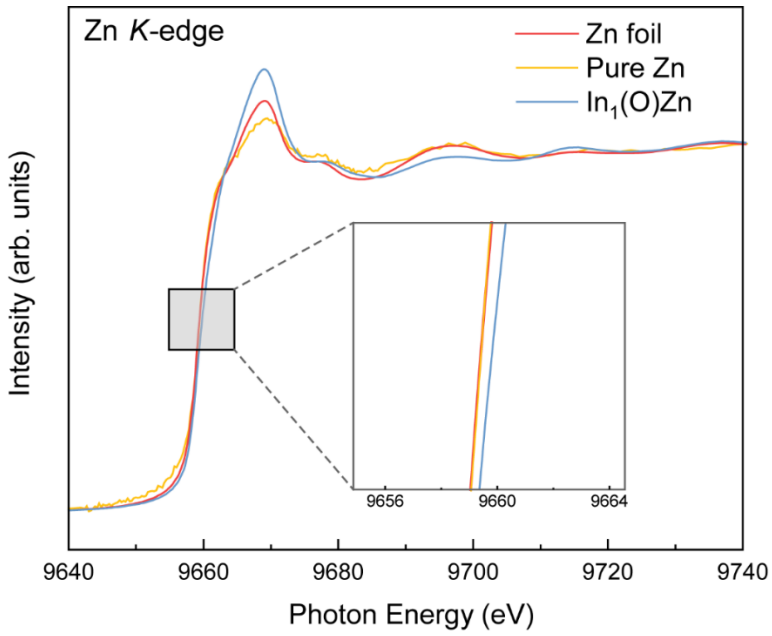

Figure S7. *Operando* Zn *K*-edge XAS profiles of pristine Zn during the CO_2RR. Compared with the In_1(O)Zn catalyst, pristine Zn tends to be easily reduced to a metallic state during the CO_2RR. This contrast evidences the electronic modulation of the Zn matrix imposed by the atomic In_1O_6 domains of the In_1(O)Zn catalyst.

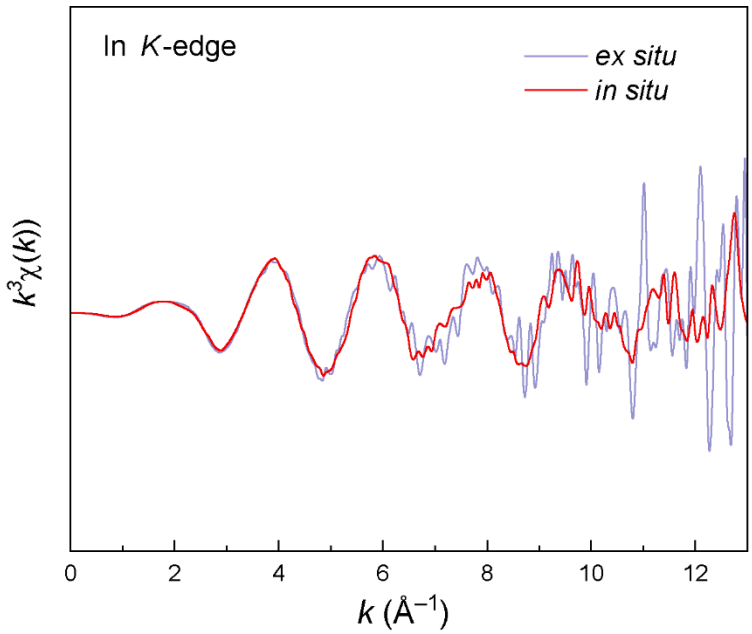

Figure S8. Comparison of *in situ* and *ex situ* $\chi(k)$ data in the *k*-space of the In$_1$(O)Zn catalyst. The results were basically the same. However, owing to the single-atom level content of In element, the signal quality was poor during *in situ* XAS analysis.

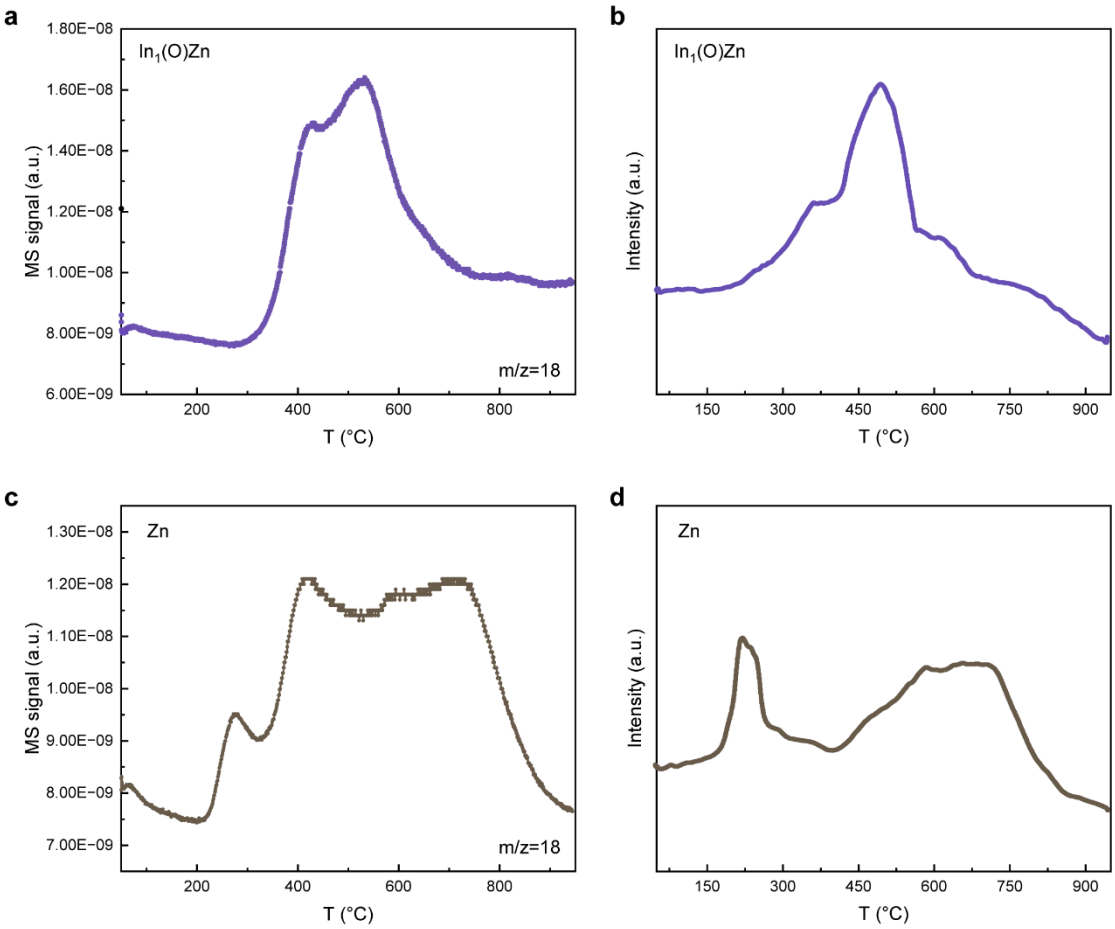

Figure S9. TPR-H_2 measurements of the In_1(O)Zn catalyst and pristine Zn. MS signal of H_2O during TPR measurements of the In_1(O)Zn catalyst (a) and pristine Zn (c). Total TPR signal intensity of the In_1(O)Zn catalyst (b) and pure Zn (d). The original oxygen content of the In_1(O)Zn catalyst was ~18.9 wt%, whereas that of the pristine-Zn was ~17.8 wt%, indicating that the In_1(O)Zn catalyst has a higher oxygen content.

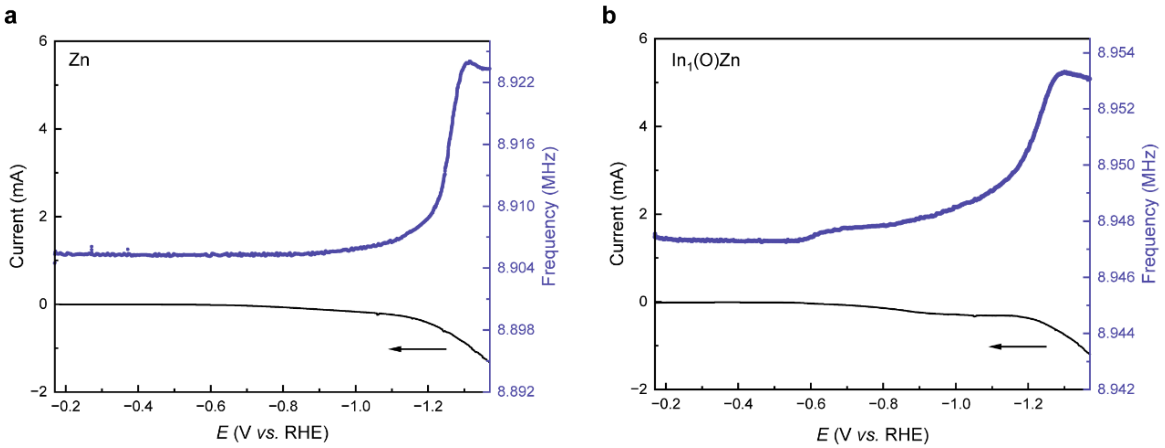

Figure S10. *In situ* electrochemical QCM experiment of the In_1(O)Zn catalyst and pristine Zn. The quantity loss (6044.2 Hz, ~7 wt%) of the In_1(O)Zn catalyst was smaller than that of pristine Zn (19573.6 Hz, ~20 wt%), inferring that the inert property of In_1(O)Zn for being reduced under cathodic potentials. No *iR* compensation was conducted.

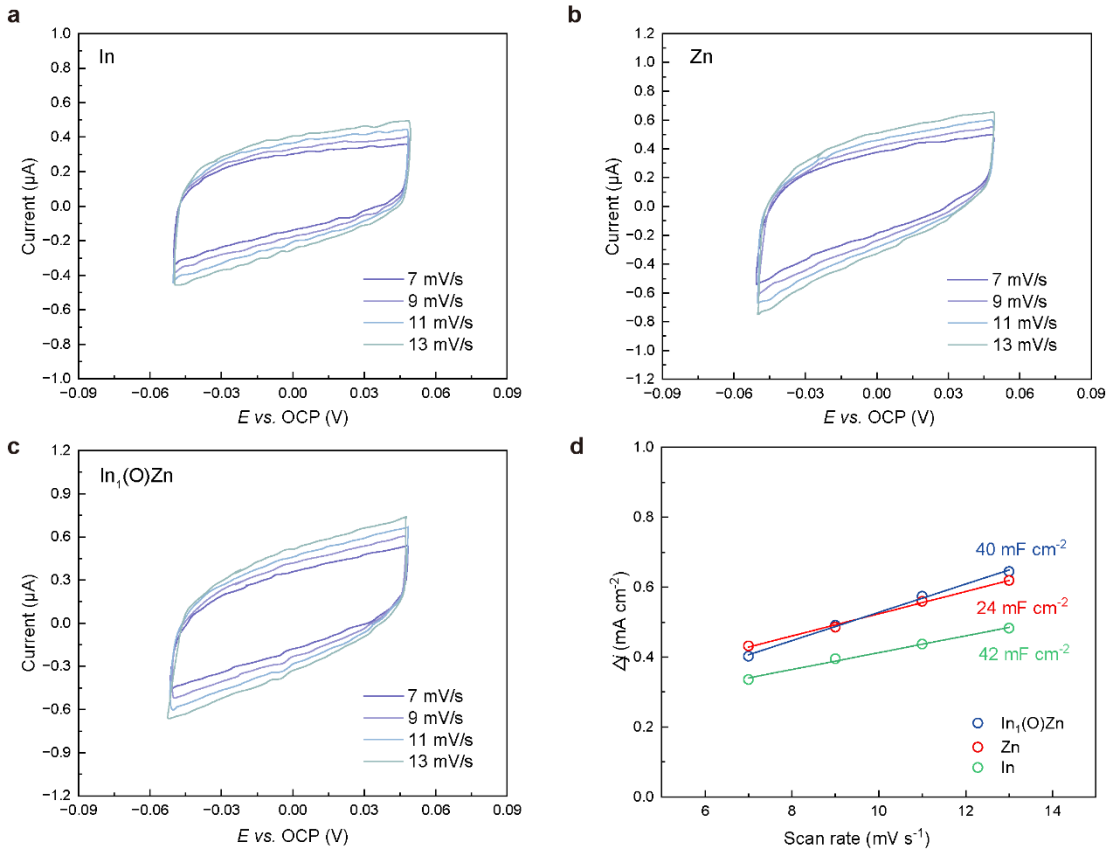

Figure S11. ECSA measurements for the pristine Zn (a), In (b) and In_1(O)Zn (c) catalysts, the results of which are shown in (d). The ECSA results were measured via the double-layer capacitance method. Considering that ion transfer reactions at the catalyst interface are particularly significant in aqueous electrolytes, which might change the capacitance values. Therefore, we conducted ECSA measurements in weakly coordinating and aprotic KF_6P/MeCN electrolytes. ECSA= C_{dl}×area/C_S, where the C_S of the Zn electrode was assumed to be 1 mF since the relative roughness factor of zinc surfaces in organic solvents has not yet been established. Given that we are only concerned with the relative values of these data rather than absolute numbers, this simplification is reasonable.

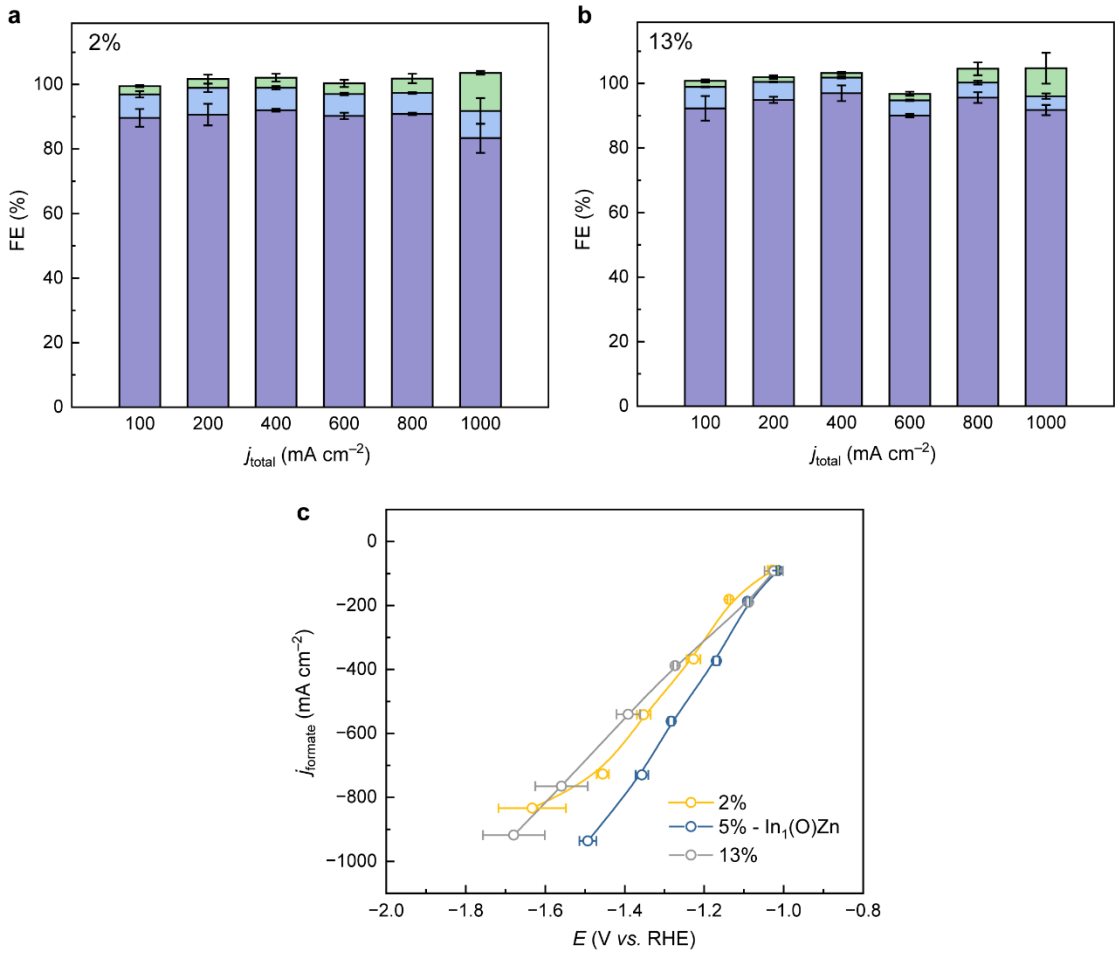

Figure S12. CO_2RR performance of the 2% and 13% In-contained samples compared with that of the In_1(O)Zn catalyst (5% In content).

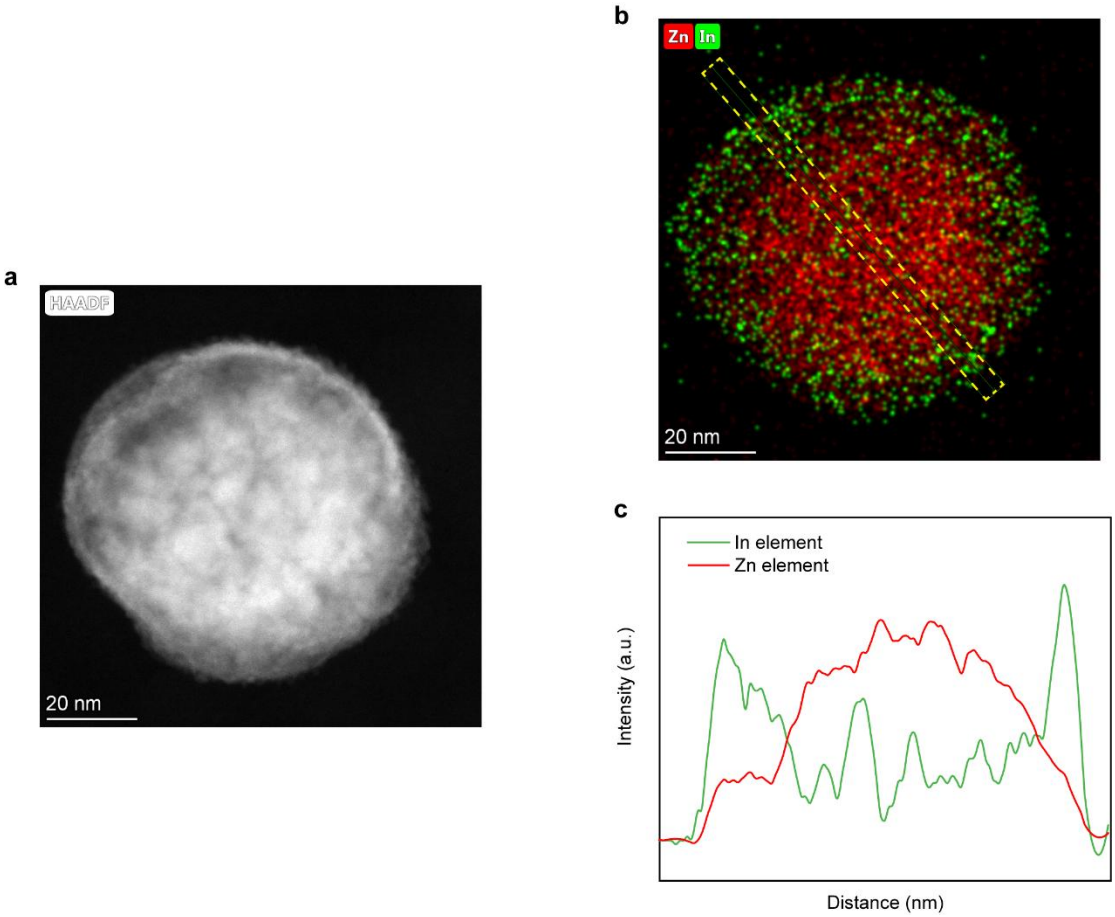

Figure S13. HAADF-STEM (a) and STEM-EDS (b) mapping of the 13% In-contained sample. (c) was derived from the elemental analysis of the linear scan in (b). The inferior CO_2RR performance is attributed to metal segregation.

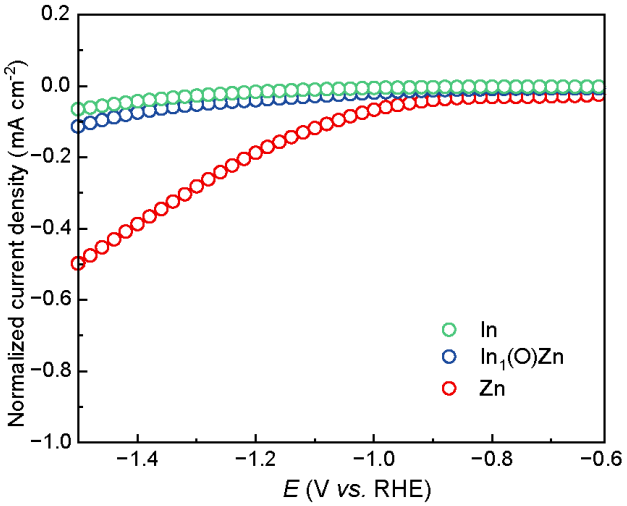

Figure S14. ECSA-normalized LSV curves of three as-synthesized catalysts during the HER.

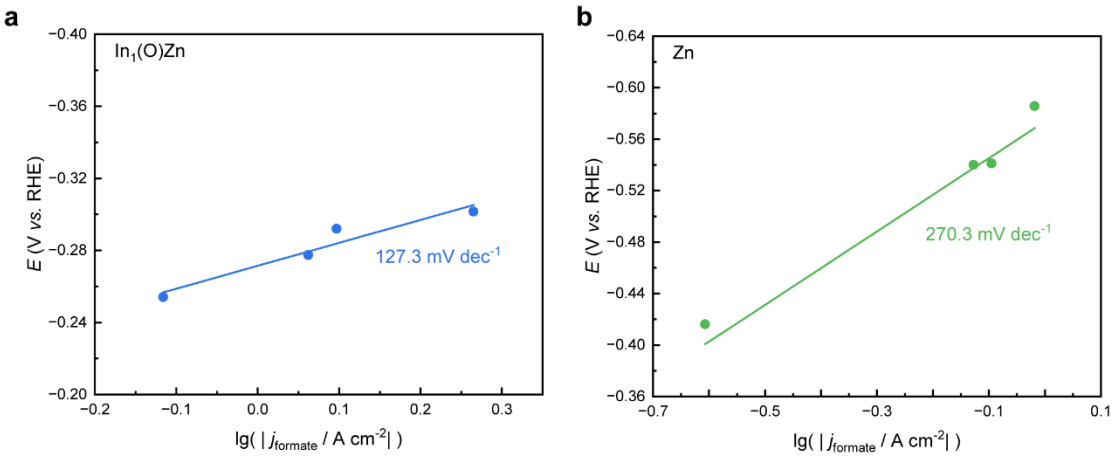

Figure S15. Tafel plots of pristine Zn and In_1(O)Zn catalysts. The Tafel value of 127.3 mV dec^{-1} for the In_1(O)Zn catalyst *vs.* 270.3 mV dec^{-1} for pristine-Zn confirmed accelerated electron transfer kinetics on In_1(O)Zn, emphasizing the indispensable role of the atomic In_1O_6 domains in increasing formate production.

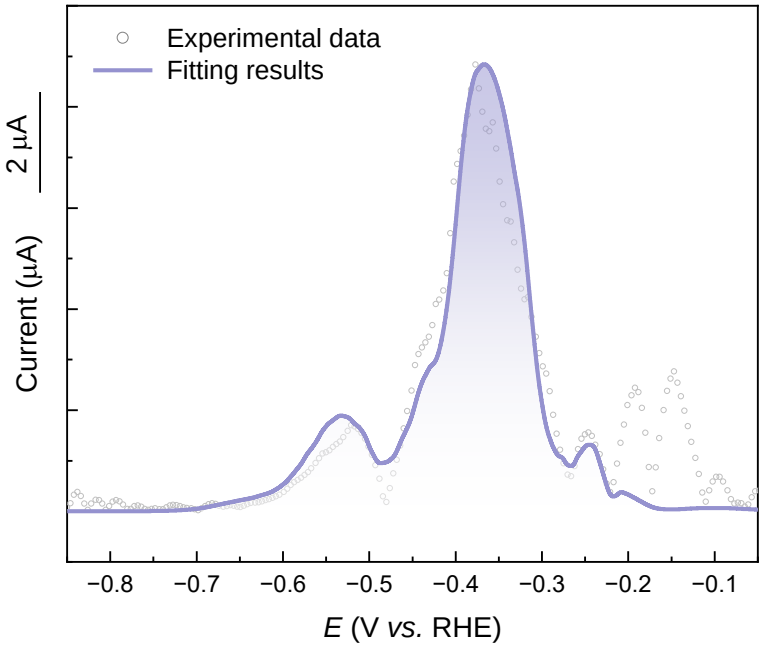

Figure S16. FTacV simulation results for the In_1(O)Zn catalyst.

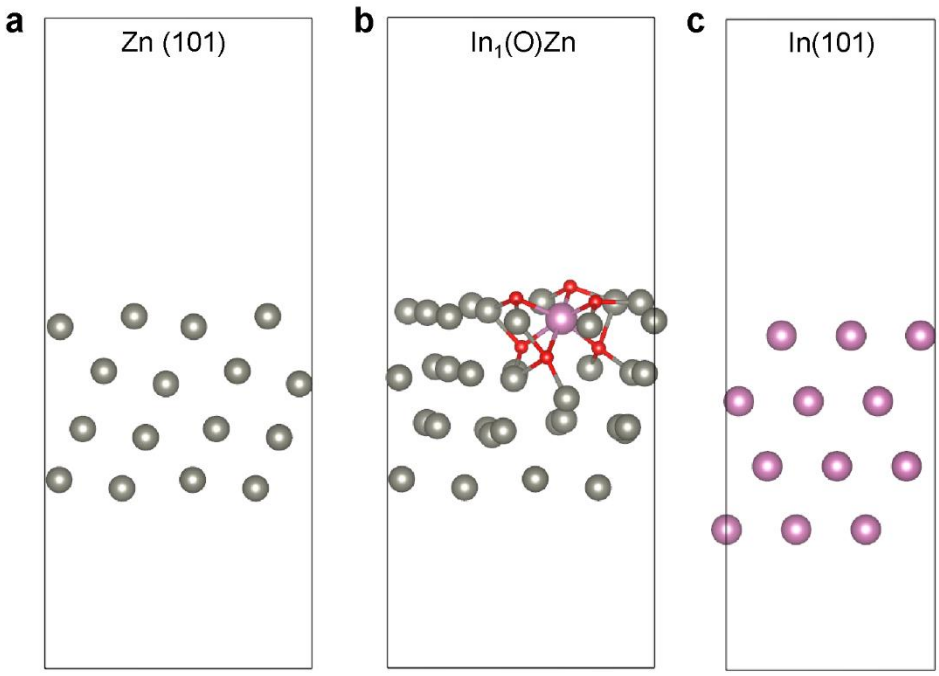

Figure S17. Optimized structures of Zn (101), In_1(O)Zn, and In (101). The grey, red, and pink atoms represent Zn, O, and In, respectively. The bottom layer of atoms of In_1(O)Zn and bottom two layers of Zn and In (101) were constrained in the calculations. A vacuum of 15 Å were introduced to these surfaces to avoid the interaction between periodically adjacent slabs.

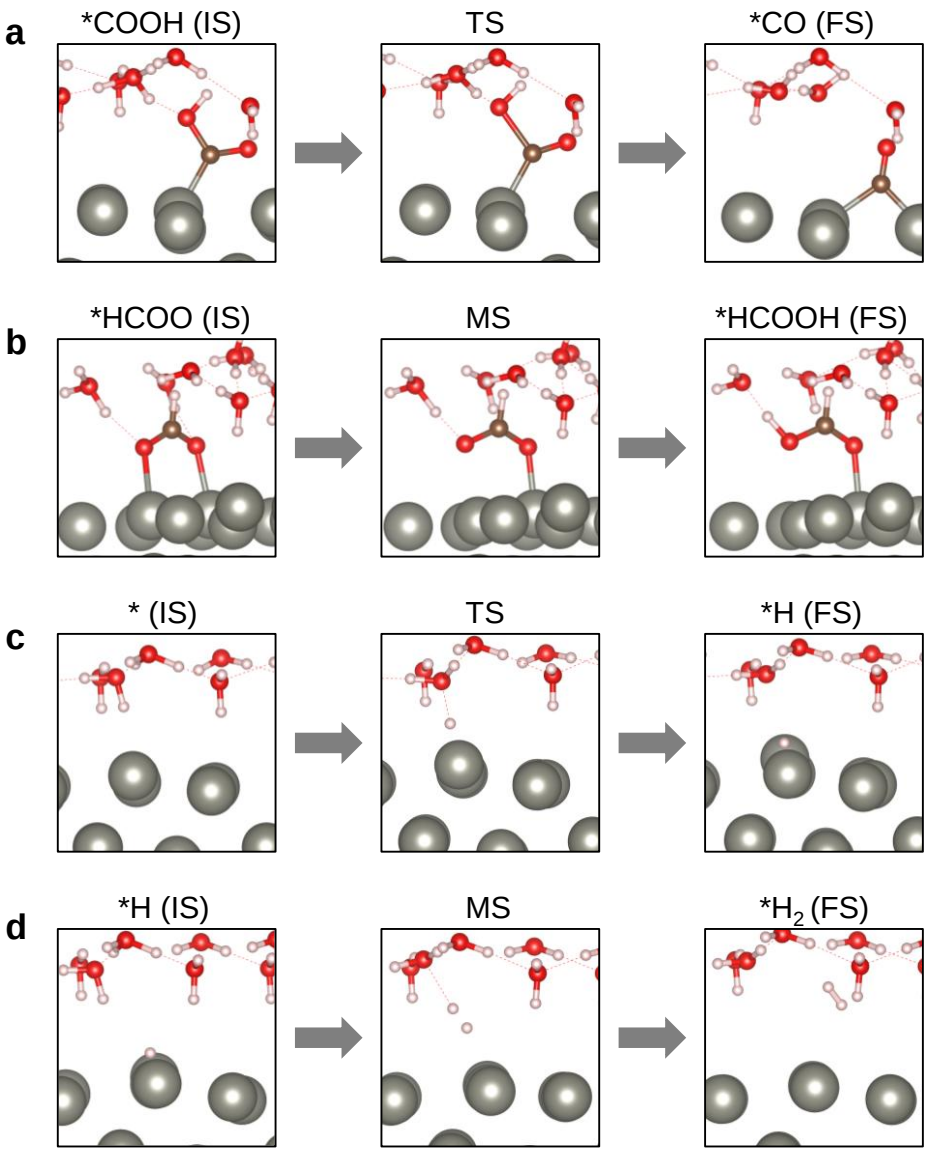

Figure S18. Computational structures of the initial state (IS), transition state (TS) [or intermediate state (MS)], and final state (FS) for different elementary steps on Zn. (a) *COOH → *CO. (**b**) *HCOO → *HCOOH. (**c**) * → *H. (**d**) *H → *H_2. For *CO_2 → *HCOO and *CO_2 → *COOH, the corresponding structures have been presented in Figure 4b. The grey, red, brown, and white atoms represent Zn, O, C, and H, respectively.

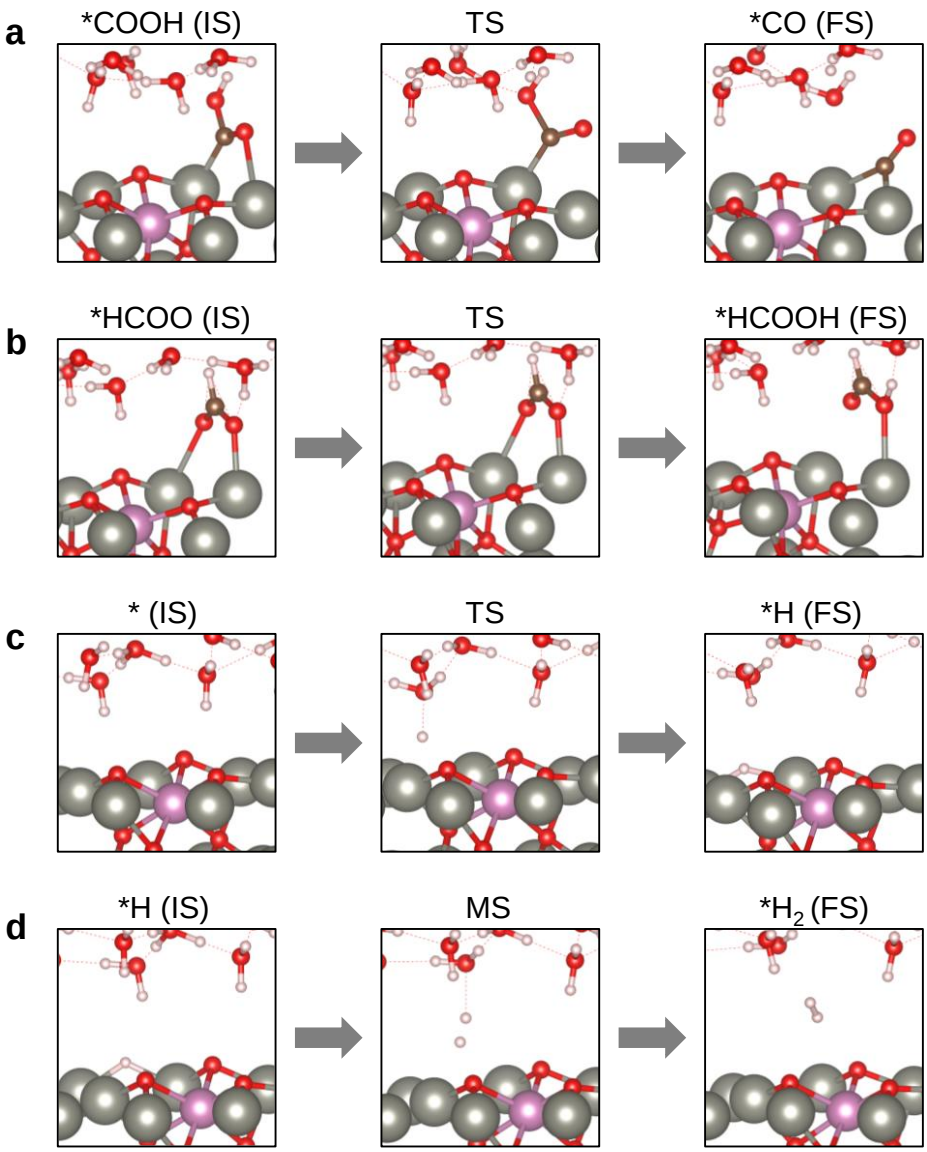

Figure S19. Computational structures of the initial state (IS), transition state (TS) [or intermediate state (MS)], and final state (FS) for different elementary steps on $In_1(O)Zn$. (a) *COOH → *CO. (**b**) *HCOO → *HCOOH. (**c**) * → *H. (**d**) *H → *H_2. For *CO_2 → *HCOO and *CO_2 → *COOH, the corresponding structures have been presented in Figure 4c. The grey, pink, red, brown, and white atoms represent Zn, In, O, C, and H, respectively.

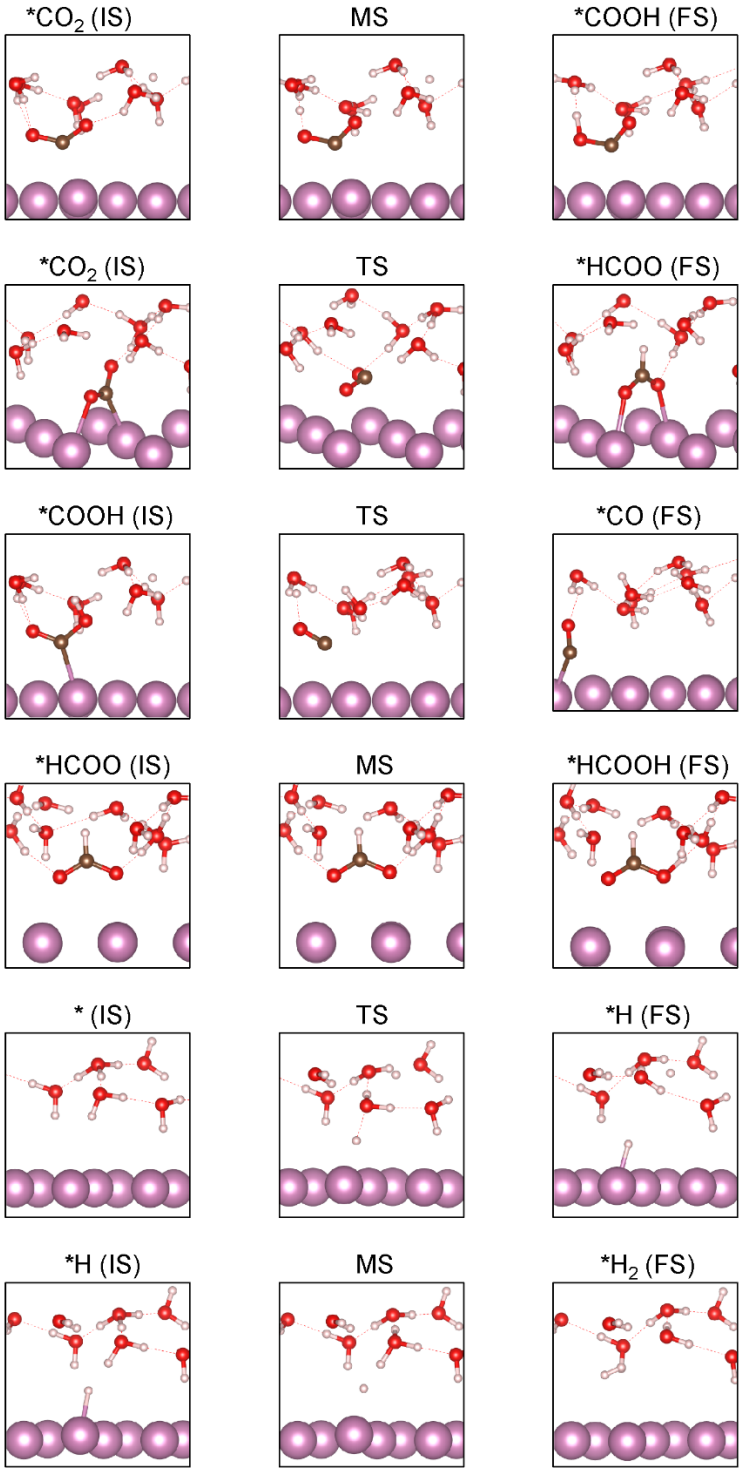

Figure S20. Computational structures of the initial state (IS), transition state (TS) [or intermediate state (MS)], and final state (FS) for different elementary steps on In. (a) *CO_2 → *COOH. **(b)** *CO_2 → *HCOO. **(c)** *COOH → *CO. **(d)** *HCOO → *HCOOH. **(e)** * → *H. **(f)** *H → *H_2. The pink, red, brown, and white atoms represent In, O, C, and H, respectively.

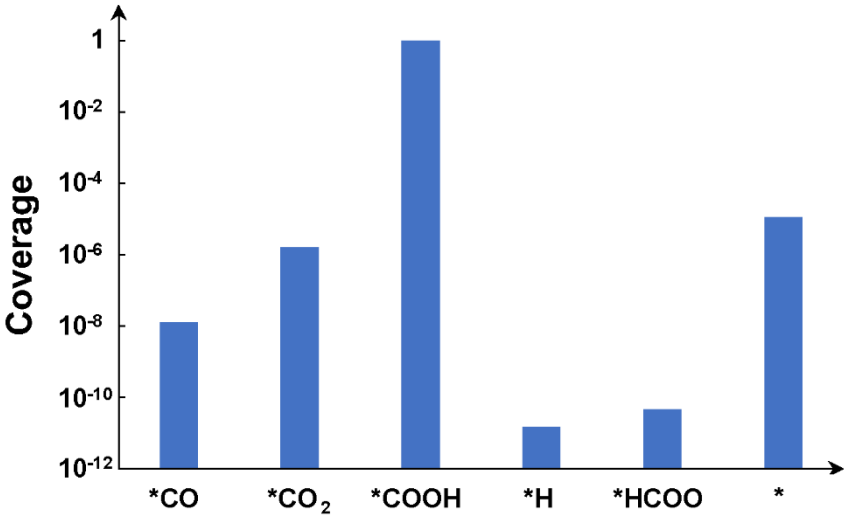

Figure S21. Surface coverage of different reaction intermediates for the CO_2RR on In obtained by microkinetic simulations.

Figure S22. Schematic illustration and the photograph of a PSE reactor.

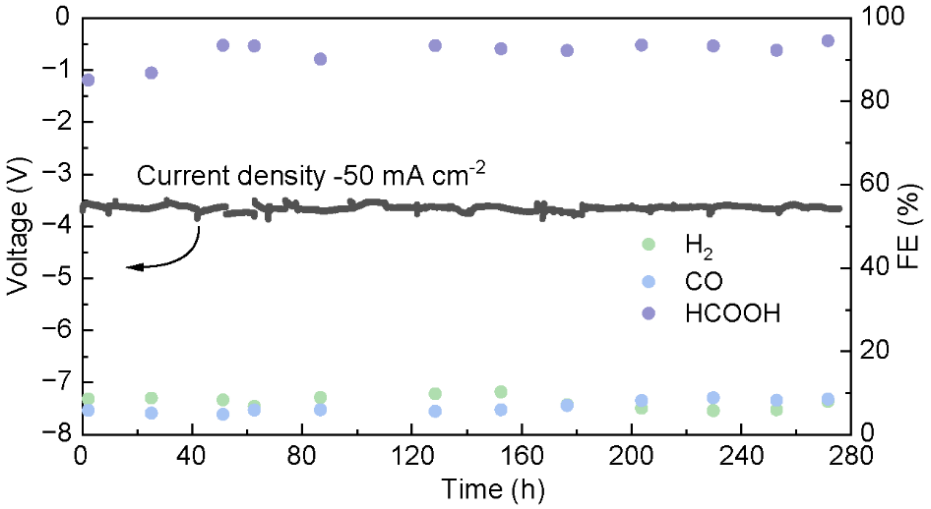

Figure S23. CO_2RR performance of the In_1(O)Zn catalyst at a current density of -50 mA cm^{-2} in a PSE reactor without *iR* corrections to the voltage.

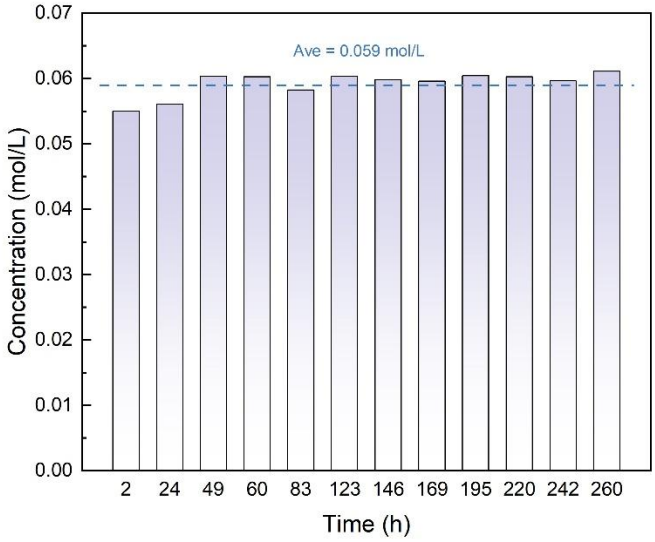

Figure S24. Concentration of pure formic acid solution produced by In_1(O)Zn catalyst during the CO_2RR in a PSE reactor. An average concentration of ~59 mM pure formic acid solution was demonstrated.

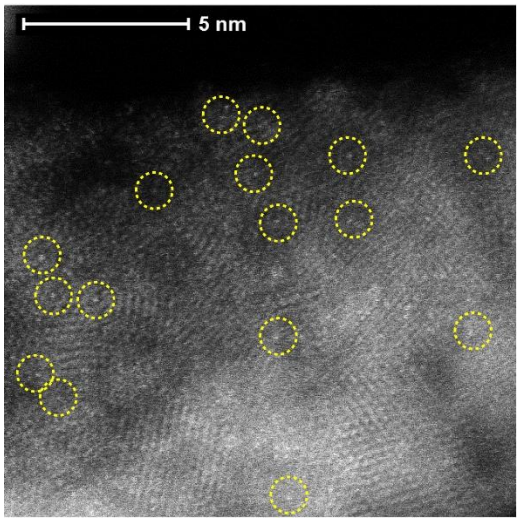

Figure S25. HAADF-STEM characterization of the In_1(O)Zn catalyst after the CO_2RR. The fully isolated dispersion of In atoms in the Zn matrix confirmed the robust structural integrity of the In_1(O)Zn catalyst.

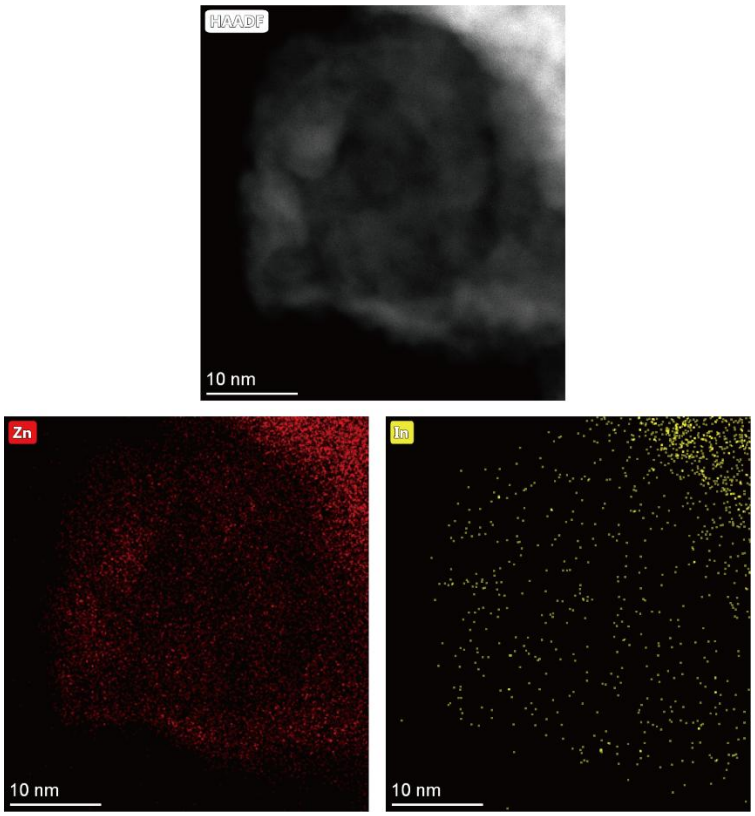

Figure S26. STEM-EDS mapping results for the In_1(O)Zn catalyst after the CO_2RR. In element is uniformly dispersed within the Zn matrix, in accordance with the HAADF-STEM results.

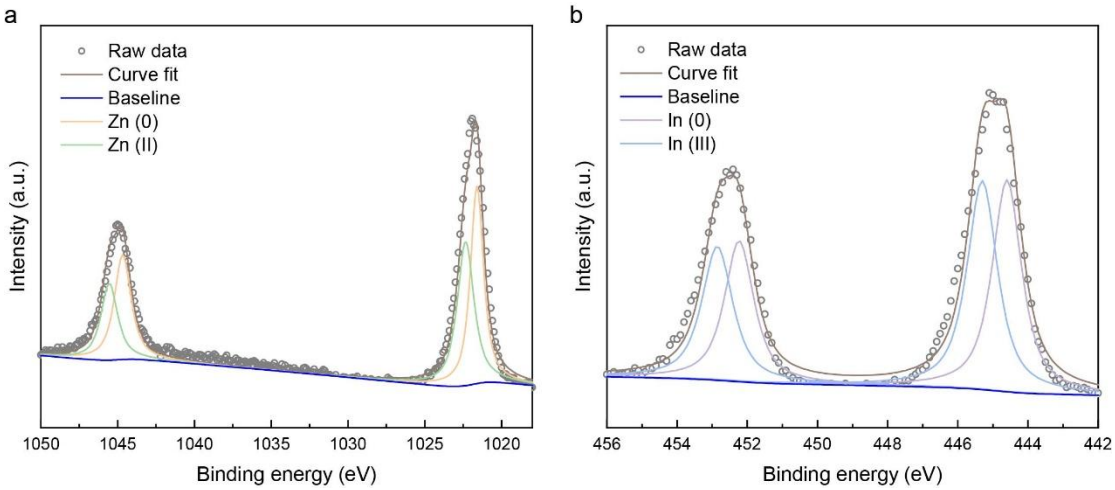

Figure S27. Post-reaction XPS analysis of In_1(O)Zn catalyst. Zn 2*p* (a) and In 3*d* (b) spectra on the catalyst surface.

Figure S28. Schematic illustration of the flow-cell configuration.

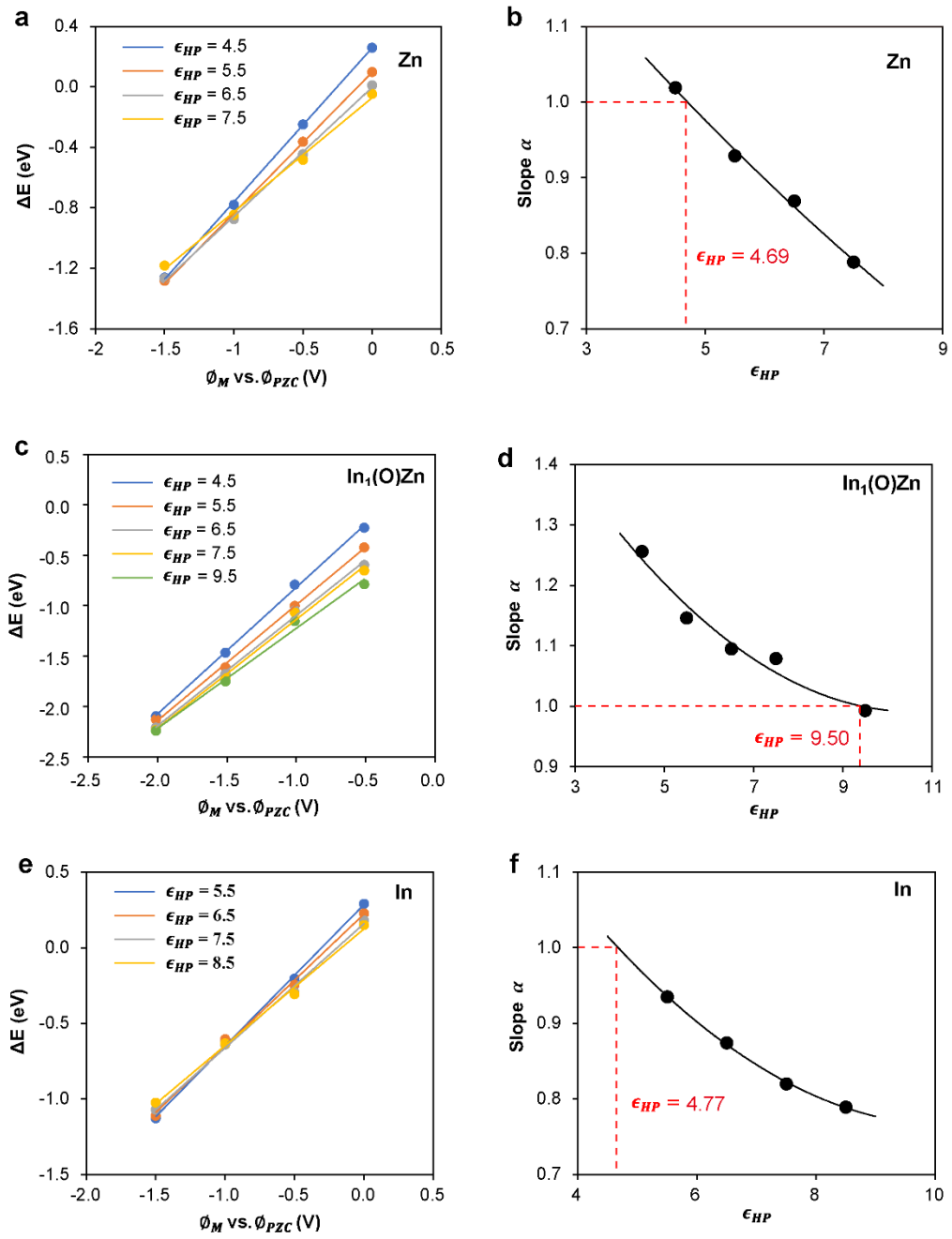

Figure S29. Fitting the dielectric constant (ϵ_{HP}) of catalyst-water interfaces. (a,c,e) Linear correlations between reaction energies of Volmer reaction and electrode potential ($\emptyset_M$) under different ϵ_{HP} for Zn, In_1(O)Zn, and In-water model, respectively. **(b,d,f)** Fitting results of ϵ_{HP} for Zn, In_1(O)Zn, and In-water model, respectively. The ϵ_{HP} was used in the EFC-CP method for electrochemical barrier calculations at constant potential.

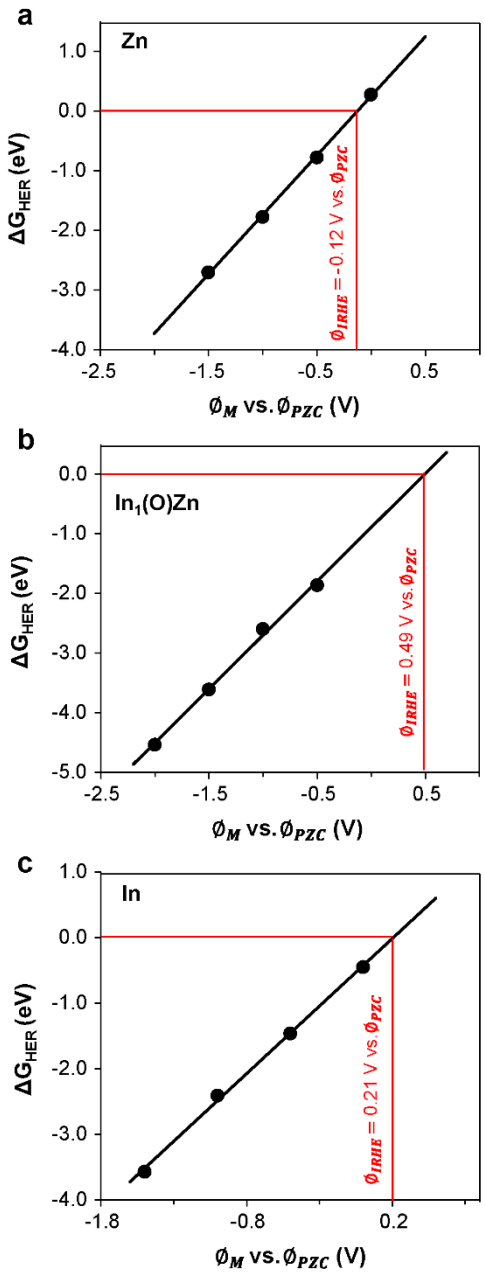

Figure S30. Fitting the $\emptyset_{IRHE}$ of catalyst-water interfaces. (a,b,c) Fitting results of $\emptyset_{IRHE}$ for Zn, In_1(O)Zn, and In-water model. Since the electrode potential ϕ_M is referenced to the potential of zero charge (ϕ_{PZC}), while the experiments usually refer the potential to hydrogen electrode. Therefore, we defined an internal reversible hydrogen electrode (IRHE) potential for a given catalyst-water interface/model, at which the explicitly computational reaction free energy of hydrogen evolution reaction (ΔG_{HER}) is zero.

Table S1. ICP-AES measurements of different samples.

	Zn content (at%)	In content (at%)
In_1(O)Zn	95.3	4.7
In(O)Zn-2%	97.7	2.3
In(O)Zn-13%	86.9	13.1

Table S2. EXAFS fitting parameters at the In *K*-edge for the In$_1$(O)Zn catalyst.

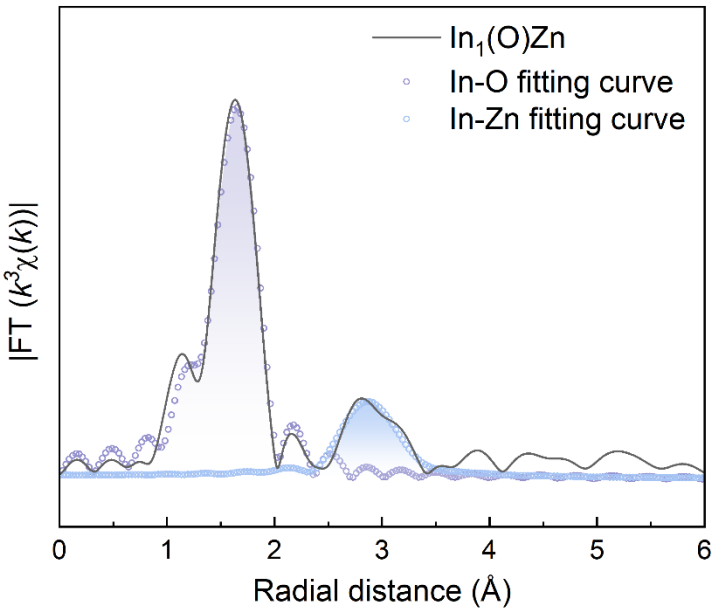

Sample	Shell	CN [a]	*R* (Å) [a]	σ^2 (Å^2) [a]	ΔE_0 (eV) [a]	*R* factor
In$_1$(O)Zn	In-O	5.8 (0.3)	2.14 (0.01)	0.005 (0.001)	3.8 (0.5)	0.007
	In-Zn	1.0 (0.7)	3.24 (0.01)	0.003 (0.004)		

[a]CN, coordination number, *R*, distance between the absorber and scatterer atoms, $\Delta\sigma^2$, disorder term, ΔE_0, inner potential correction. Details of the data analysis: *k* range: 2.30-11.70 Å^{-1}, *R* range: 1.0-3.5 Å. Error is reported inside the parentheses (accuracies). The S_0^2 term was determined to be 0.83 by fitting In_2O_3.

Table S3. Comparison of the PCE performances of state-of-the-art catalysts with $In_1(O)Zn$ catalyst.

Catalyst	*j* (mA cm^{-2})	PCE (%)	References
$In_1(O)Zn$	*-100*	*54*	*This work*
	-200	52	
	-1000	~45	
Bi@Sn NPs	-2	~48	14
Sn NPs	-20	~38	14
$ZnIn_2S_4$	-200	51	15
In_2S_3	-180	45	15
Sn based GDE	-163	32 (Full cell)	16
Sn 3D electrode	-133	33 (Full cell)	17

Table S4. Tafel slopes for different possible RDSs during CO_2-to-formate conversion (assuming $\alpha = 0.5$).

Possible RDSs	Type	Tafel slope (mV dec^{-1})
$CO_2 + * + e^- \rightarrow *CO_2^-$	Electron transfer	118
$*CO_2^- + H_2O \rightarrow HCOO* + OH^-$	Proton transfer	59
$HCOO* + e^- \rightarrow HCOO*^-$	Electron transfer	39
$HCOO*^- \rightarrow HCOO^- + *$	Desorption	30

Table S5. The lengths of the In-O and In-Zn bonds in the $In_1(O)Zn$ model after structural optimization.

	In-O bond (Å)	In-Zn bond (Å)
Bond 1	2.20	3.08
Bond 2	2.20	3.31
Bond 3	2.14	3.09
Bond 4	2.32	3.45
Bond 5	2.23	3.34
Bond 6	2.37	3.16
Average	**2.24**	**3.24**
Experiment	**2.14**	**3.24**

Table S6. Adsorption energies (eV) of different reaction intermediates on Zn, $In_1(O)Zn$, and In.

	*CO_2	*HCOO	*COOH	*CO	*H
Zn	-0.42	-0.95	-0.18	0.07	0.06
$In_1(O)Zn$	-0.26	-0.76	0.22	0.62	0.17
In	-0.44	-1.26	0.35	0.56	0.24

Table S7. Stability of many reported bulk Sn/Bi/In-based catalysts in the CO_2RR.

Cathode	Catholyte	Cell structure	Current density (mA cm^{-2})	$FE_{formate}$ (%)	Stability (h)	Ref.
In_1(O)Zn	*None*	*PSE*	*-50*	*90*	*260*	*This work*
Bi-PNS	0.5 M $KHCO_3$	H-cell	-47.5	95	9	18
Sn SA/ZnO	0.5 M $KHCO_3$	Flow cell	~-80	80	11	19
SnIn-3	0.1 M $KHCO_3$	Flow cell	-38	80	58	20
Zn(Pb)	0.5 M $KHCO_3$	Flow cell	-100	30	5	21
nBuLi-Bi	None	PSE	-30	80	50	22
Bismuthene nanosheets	1 M $KHCO_3$	Flow cell	-50	Not reported	25	23
Bi-Sn	0.1 M $KHCO_3$	Flow cell	-10	>75	10	24
Bi-MOF	0.1 M $KHCO_3$	H-cell	-5	92	30	25
BMNS	0.5 M $KHCO_3$	H-cell	-20	95	40	26
BBS	1 M KOH	Flow cell	-40	80	2.8	27

Supplementary References

1 Ma, W., Bu, J., Liu, Z., Yan, C., Yao, Y., Chang, N., Zhang, H., Wang, T., Zhang, J., Monoclinic Scheelite Bismuth Vanadate Derived Bismuthene Nanosheets with Rapid Kinetics for Electrochemically Reducing Carbon Dioxide to Formate. *Advanced Functional Materials* **2020**, *31*(4).

2 Kresse, G., Furthmuller, J. Efficient iterative schemes for ab initio total-energy calculations using a plane-wave basis set. *Physical Review B* **1996**, *54*, 11169-11186.

3 Kresse, G., Furthmuller, J. Efficiency of ab-initio total energy calculations for metals and semiconductors using a plane-wave basis set. *Computational Materials Science* **1996**, *6*, 15-50.

4 Zhang, Y. K., Yang, W. T. Comment on "Generalized gradient approximation made simple". *Physical Review Letters* **1998**, *80*, 890-890.

5 Grimme, S. Semiempirical GGA-type density functional constructed with a long-range dispersion correction. *Journal of Computational Chemistry* **2006**, *27*, 1787-1799.

6 Henkelman, G., Jónsson, H. Improved tangent estimate in the nudged elastic band method for finding minimum energy paths and saddle points. *Journal of Chemical Physics* **2000**, *113*, 9978-9985.

7 Henkelman, G., Uberuaga, B. P., JóNsson, H. A Climbing Image Nudged Elastic Band Method for Finding Saddle Points and Minimum Energy Paths. *Journal of Chemical Physics* **2000**, *113*, 9901-9904.

8 Luan, D., Xiao, J. Adaptive Electric Fields Embedded Electrochemical Barrier Calculations. *Journal of Physical Chemistry Letters* **2023**, *14*, 685-693.

9 Won da, H., Shin, H., Koh, J., Chung, J., Lee, H. S., Kim, H., Woo, S. I. Highly Efficient, Selective, and Stable CO_2 Electroreduction on a Hexagonal Zn Catalyst. *Angewandte Chemie International Edition* **2016**, *55*, 9297-300.

10 Wei, B., Xiong, Y., Zhang, Z., Hao, J., Li, L., Shi, W. Efficient electrocatalytic reduction of CO_2 to HCOOH by bimetallic In-Cu nanoparticles with controlled growth facet. *Applied Catalysis B: Environmental* **2021**, *283*, 119646.

11 Ma, W., Xie, S., Zhang, X. G., Sun, F., Kang, J., Jiang, Z., Zhang, Q., Wu, D. Y., Wang, Y. Promoting electrocatalytic CO_2 reduction to formate via sulfur-boosting water activation on indium surfaces. *Nature Communications* **2019**, *10*, 892.

12 Chen, J., Jia, M., Hu, P., Wang, H. CATKINAS: A large-scale catalytic microkinetic analysis software for mechanism auto-analysis and catalyst screening. *Journal of Computational Chemistry* **2021**, *42*, 379-391.

13 Chen, J.-F., Mao, Y., Wang, H.-F., Hu, P. Reversibility Iteration Method for Understanding Reaction Networks and for Solving Microkinetics in Heterogeneous Catalysis. *ACS Catalysis* **2016**, *6*, 7078-7087.

14 Xing, Y., Kong, X., Guo, X., Liu, Y., Li, Q., Zhang, Y., Sheng, Y., Yang, X., Geng, Z., Zeng, J., Bi@Sn Core-Shell Structure with Compressive Strain Boosts the Electroreduction of CO_2 into Formic Acid. *Adv Sci* **2020**, *7* (22), 1902989.

15 Chi, L. P., Niu, Z. Z., Zhang, X. L., Yang, P. P., Liao, J., Gao, F. Y., Wu, Z. Z., Tang, K. B., Gao, M. R., Stabilizing indium sulfide for CO_2 electroreduction to formate at high rate by zinc incorporation. *Nat Commun* **2021**, *12* (1), 5835.

16 Whipple, D. T., Finke, E. C., Kenis, P. J., Microfluidic Reactor for the Electrochemical Reduction of Carbon Dioxide: The Effect of pH. *Electrochem. Solid-State Lett.* **2010**,

13 (9), B109-B111.

17 Li, H., Oloman, C., Development of a continuous reactor for the electro-reduction of carbon dioxide to formate - Part 1: Process variables. *J. Appl. Electrochem.* **2006**, *36*, 1105-1115.

18 Yu, Z. L., Wu, S. Q., Chen, L. W., Hao, Y. C., Su, X., Zhu, Z., Gao, W. Y., Wang, B., Yin, A. X., Promoting the Electrocatalytic Reduction of CO_2 on Ultrathin Porous Bismuth Nanosheets with Tunable Surface-Active Sites and Local pH Environments. *ACS Applied Materials & Interfaces* **2022,** *14* (8), 10648-10655.

19 Zhang, Y., Jang, H., Ge, X., Zhang, W., Li, Z., Hou, L., Zhai, L., Wei, X., Wang, Z., Kim, M. G., Liu, S., Qin, Q., Liu, X., Cho, J., Single-Atom Sn on Tensile-Strained ZnO Nanosheets for Highly Efficient Conversion of CO_2 into Formate. *Advanced Energy Materials* **2022,** *12* (45).

20 Wang, J., Ning, S., Luo, M., Xiang, D., Chen, W., Kang, X., Jiang, Z., Chen, S., In-Sn alloy core-shell nanoparticles: In-doped SnOx shell enables high stability and activity towards selective formate production from electrochemical reduction of CO_2. *Applied Catalysis B: Environmental* **2021,** *288*.

21 Mohamed, A. G. A., Zhou, E., Zeng, Z., Xie, J., Gao, D., Wang, Y., Asymmetric Oxo-Bridged ZnPb Bimetallic Electrocatalysis Boosting CO_2-to-HCOOH Reduction. *Advanced Science* **2022,** *9* (4), e2104138.

22 Fan, L., Xia, C., Zhu, P., Lu, Y., Wang, H., Electrochemical CO_2 reduction to high-concentration pure formic acid solutions in an all-solid-state reactor. *Nature Communications* **2020,** *11* (1), 3633.

23 Ma, W., Bu, J., Liu, Z., Yan, C., Yao, Y., Chang, N., Zhang, H., Wang, T., Zhang, J., Monoclinic Scheelite Bismuth Vanadate Derived Bismuthene Nanosheets with Rapid Kinetics for Electrochemically Reducing Carbon Dioxide to Formate. *Advanced Functional Materials* **2020,** *31* (4).

24 Wu, Z., Wu, H., Cai, W., Wen, Z., Jia, B., Wang, L., Jin, W., Ma, T., Engineering Bismuth-Tin Interface in Bimetallic Aerogel with a 3D Porous Structure for Highly Selective Electrocatalytic CO_2 Reduction to HCOOH. *Angewandte Chemie International Edition* **2021,** *60* (22), 12554-12559.

25 Li, F., Gu, G. H., Choi, C., Kolla, P., Hong, S., Wu, T.-S., Soo, Y.-L., Masa, J., Mukerjee, S., Jung, Y., Qiu, J., Sun, Z., Highly stable two-dimensional bismuth metal-organic frameworks for efficient electrochemical reduction of CO_2. *Applied Catalysis B: Environmental* **2020,** *277*.

26 Li, N., Yan, P., Tang, Y., Wang, J., Yu, X.-Y., Wu, H. B., In-situ formation of ligand-stabilized bismuth nanosheets for efficient CO_2 conversion. *Applied Catalysis B: Environmental* **2021,** *297*.

27 Lv, L., Lu, R., Zhu, J., Yu, R., Zhang, W., Cui, E., Chen, X., Dai, Y., Cui, L., Li, J., Zhou, L., Chen, W., Wang, Z., Mai, L., Coordinating the Edge Defects of Bismuth with Sulfur for Enhanced CO_2 Electroreduction to Formate. *Angewandte Chemie International Edition* **2023,** *62* (25), e202303117.